IEEE Robotics and Automation Letters (RA-L) paper, presented at ICRA 2026, Vienna, Austria. Cite as RA-L paper.

A Continuum Robot With Programmable Tendon Routing for Desired Curve Generation

Kehong Zhou, *Graduate Student Member, IEEE*, Lifeng Zhu, *Member, IEEE*, Jinfeng Wu, *Graduate Student Member, IEEE*, Yurui Wen, Aiguo Song, *Senior Member, IEEE*, and Yongjie Jessica Zhang

***Abstract*—Continuum robots are widely employed in confined environments with narrow passages and spatial constraints. However, achieving general curves with non-constant curvature remains challenging, as existing systems typically rely on multiple flexible segments arranged in series, coupled with complex drive systems requiring numerous actuators. This letter proposes a novel continuum robot design that features a programmable tendon routing capable of generating desired curves. The system integrates modular joints and a single-actuator drive unit, enabling the generation of spatial curves with non-constant curvature. By strategically designing the arrangement of modular joints to control rotational direction and angular deflection at each joint, the system achieves a substantially expanded design workspace compared to conventional continuum robots. Simulation and prototype experiments validate the proposed design methodology. The relative mean distance between simulated and desired curve remains below 3.12%, while the prototype demonstrates a relative mean distance of 6.67% from the desired curve. This approach offers a promising pathway to advance continuum robot design by improving configurational adaptability while simultaneously achieving complex curve generation and reduced drive system complexity.**

***Index Terms*—Continuum robot, programmable structure, wire-driven actuation, modular joint.**

I. Introduction

THE continuum robot, a slender, actuatable structure characterized by continuous tangent vectors [1], is widely used in applications such as medical procedures [2], underground tunnel exploration [3], and underwater tasks [4]. To operate effectively in narrow, constrained environments, continuum robots typically employ 1–3 bendable segments actuated by wires [5], air pumps [6], or magnetic actuators [7]. Among the designs, wire-driven continuum robots are a research focus due to their stability, lightweight design, and fabrication simplicity [3]. Common wire-driven continuum robots include multi-joint structures [8], [9], [10], notch-based designs [11], [12], and integrated flexible structures [13], [14]. These continuum robots contain 2–3 segments. Each segment uses 1–4 dedicated actuators to form constant-curvature arcs. However, their motion trajectories remain limited to 2–3 constant-curvature segments. This constraint causes increased control complexity and kinematic limitations in unstructured environments.

To address these limitations, asymmetric continuum robot designs are developed to enhance dexterity and workspace [15], including helical cable routing [16], [17], twisted tendon routing [18], constrained joint-bending mechanisms [19], [20], and actuator-minimizing optimizations [21]. However, these methods lack inverse optimization frameworks to derive robot configurations from task-space trajectories. 3D-printed cable-driven fabrication methods [22] require tendons to remain straight in their undriven state due to printing process constraints, which limits achievable workspace flexibility. While asymmetric continuum robots [23] achieve trajectory-specific tendon arrangements, their 16-motor system for four-segment actuation illustrates the challenge of balancing scalability and mechanical simplicity. To address this, our parametric design framework, which is defined by yaw angle α and pitch angle θ, enables systematic exploration of geometric configurations while reducing reliance on complex actuation systems. This approach facilitates performance optimization in constrained environments through simplified mechanical design.

Programmable continuum robots employ modular architectures to generate task-specific curves for specialized operations, adapting to targeted geometric profiles, stiffness distributions, and spatial anisotropy. For instance, modular morphing lattices [4] enable controlled local anisotropies for underwater applications, while modular tensegrity structures [24] achieve programmable stiffness through prestressed components. However, the complexity of these modular systems limits their practicality in streamlined or constrained settings. Similarly, programmable ferromagnetic robots [7] excel in end-effector dexterity but prioritize tip control over maintaining stable global

Received 31 May 2025; accepted 8 December 2025. Date of publication 16 January 2026; date of current version 2 February 2026. This article was recommended for publication by Associate Editor N. Gravish and Editor Y.-L. Park upon evaluation of the reviewers' comments. This work was supported in part by the NSFC under Grant 62133009, in part by the Natural Science Foundation of Jiangsu Province Major Project under Grant BK20232008, in part by Jiangsu Key Research and Development Plan under Grant BE2023023-4, in part by the Shenzhen Science and Technology Research under Grant JCYJ20230807142300002, and in part by the Fundamental Research Funds for the Central Universities. *(Corresponding author: Lifeng Zhu.)*

Kehong Zhou, Lifeng Zhu, Jinfeng Wu, and Aiguo Song are with the State Key Laboratory of Digital Medical Engineering, Jiangsu Key Lab of Remote Measurement and Control, School of Instrument Science and Engineering, Southeast University, Nanjing 210096, China (e-mail: zhoukh97@163.com; lfzhulf@gmail.com; 220243736@seu.edu.cn; a.g.song@seu.edu.cn).

Yurui Wen is with Future Technology Institute, Southeast University, Nanjing 210096, China (e-mail: 213233964@seu.edu.cn).

Yongjie Jessica Zhang is with the Computational Bio-modeling Laboratory, Department of Mechanical Engineering, Carnegie Mellon University, Pittsburgh, PA 15213 USA (e-mail: jessicaz@andrew.cmu.edu).

Digital Object Identifier 10.1109/LRA.2026.3655213

IEEE Robotics and Automation Letters (RA-L) paper, presented at ICRA 2026, Vienna, Austria. Cite as RA-L paper.

TABLE I
COMPARISON OF THE PROPOSED CONTINUUM ROBOT WITH OTHER WIRE-DRIVEN CONTINUUM ROBOTS

Designer	Method	Actuator number	Design variables[1]	Size[2]
Starke et al. [16]	Helical cable routing	2	1	14 × 140
Rucker et al. [18]	Twisted tendon tendon routing	1	0	20 × 242
Ai et al. [20]	Constrained joint-bending mechanisms	4	1	6 × 80
Case et al. [21]	Reduced-actuator continuum robots	8	1	34 × 240
Zeng et al. [12]	Notch design based on capstan equation	2	0	3 × 36
Zhang et al. [24]	Modular architectures	3	1	60 × 360
Barrientos-Diez et al. [23]	Asymmetric robot with task-oriented design	16	1	12 × 204
This article	Programmable tendon routing	1	2	10 × 490

[1]: The design variables characterize the flexibility in the yaw and pitch dimensions of the continuum robot's design.
[2]: The size is given in diameter (mm) × length (mm).

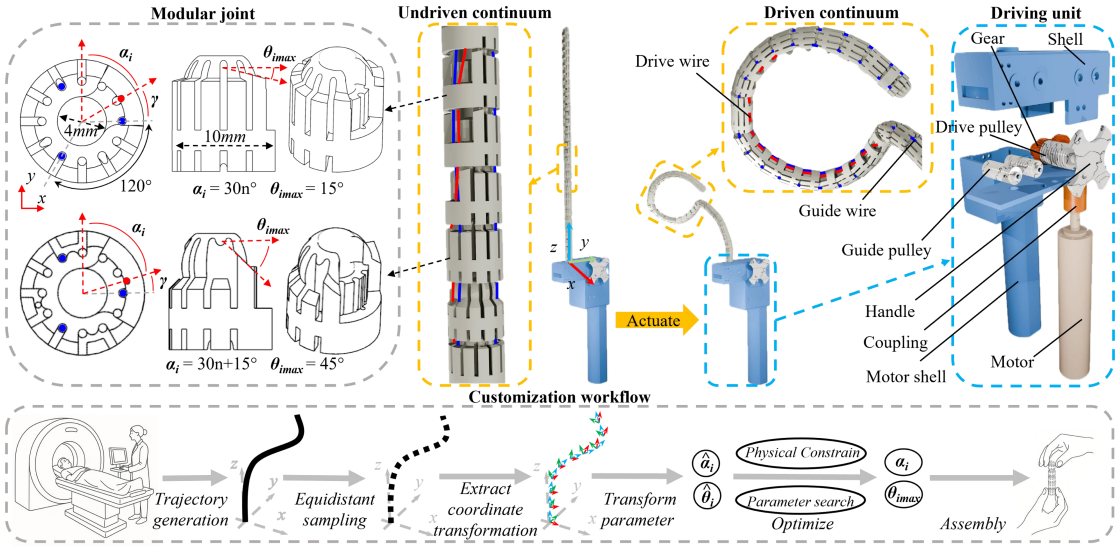

Fig. 1. The proposed continuum robot consists of modular joints and a drive unit. The red and blue lines, which connect the modular joints, represent the drive wire and guide wires, respectively, in the wire-driven system. The system is actuated by a single drive wire and constrained by three guide wires. By optimizing the α_i and θ_i of the joints and assembling different modular joints, the continuum robot can generate a specific 3D curve using a single motor. The customization workflow follows three steps. First, the desired trajectory is obtained from CT scans or other methods [25]. Then, the desired curve is processed and transformed into $\hat{\alpha}_i$ and $\hat{\theta}_i$, which are subsequently optimized to α_i and $\theta_{i\max}$. Finally, the continuum robot is assembled based on the optimized results.

curvature configurations, restricting its application in tasks requiring sustained shape retention.

In this letter, we introduce a continuum robot with a programmable tendon routing architecture capable of achieving desired spatial trajectories. The system utilizes variable-curvature kinematic modeling to generate predefined pathways through interconnected modular joints driven by a single drive wire, allowing operations within confined narrow channels. As shown in Table I, compared to existing continuum robots, the proposed design exhibits enhanced configurational adaptability and simplified actuation mechanisms, enabling task-specific configurations while maintaining operational precision. The key contributions of our design can be summarized as follows:

1) A novel programmable tendon routing architecture is developed, enabling single-actuator-driven generation of spatial curves with non-constant curvature.
2) A kinematic framework is proposed, expanding configurational adaptability of continuum robots and enabling task-specific customization by parameter optimization.
3) Modular joints are adopted to implement the continuum robot, facilitating the physical realization of the programmable tendon routing through standardized interfaces and streamlined assembly process.

II. MATERIALS AND METHODS

A. Design Consideration

1) Design Principle: We propose a continuum robot with a programmable tendon routing that is capable of generating spatial curves with variable curvature, as illustrated in Fig. 1. The proposed wire-driven continuum robot consists of a driving unit with a motor and multiple modular joints. Each modular joint has two key parameters: the yaw angle α and the pitch angle θ. α determines the direction of rotation, while θ controls the radius of the rotation in the continuum robot. Therefore, the system can be parameterized as a set of α and θ values. By adjusting α_i and θ_i for a continuum robot with i joints, the overall shape of the robot can be optimized. Base on modular joints with specific α_i and θ_i, the proposed continuum robot yields complex spatial curves with non-constant curvature using a single motor and a single drive wire.

2) Modular Joints: To facilitate the adjustment of α and θ, the modular joints are designed with articulated ball connections that provide higher DoFs for yaw and pitch motion. The proposed continuum robot incorporates two types of wires: drive wire and guide wires. The drive wire is responsible for defining α, as the rotation direction corresponds to the direction

IEEE Robotics and Automation Letters (RA-L) paper, presented at ICRA 2026, Vienna, Austria. Cite as RA-L paper.

of the applied pulling force. This wire passes through the drive hole located at the center of the joint notch, ensuring precise angular control. The guide wires serve to connect the joints in series while constraining their axial rotation. To achieve uniform load distribution and rotational stability, three guide wires are evenly distributed and routed through small peripheral holes in the modular joints. As shown in Fig. 1, there are 12 guide holes around each modular joint, with an angular spacing of 30° between adjacent holes. When the drive hole is aligned with one of the guide holes, the angle between the drive hole and the adjacent guide hole is $\gamma = 30°$, allowing the joint to operate with $\alpha = 30n°$ ($n \in N$). By subdividing γ, more types of joints can be obtained. In this letter, the values of γ are 15° and 30°. Additionally, the maximum value of θ is constrained by the tilt angle of the brake.

3) Potential Application: Compared to reconfigurable continuum robots, the proposed design lacks online adaptability. However, this represents a deliberate design trade-off. By prioritizing a fixed configuration, the system emphasizes operational stability and task specificity, which are well-suited for customization tasks in unstructured environments, such as natural orifice surgeries. In these procedures, where the path can be pre-operatively planned, the proposed robot avoids the control complexity associated with multi-actuator systems. Instead, it leverages its fixed tendon routing to effectively maintain stable operation in narrow, long passages, as shown in Table I. This approach ensures targeted performance in such scenarios while offering the capability to generate customized trajectories. Furthermore, the entire customization process, from parameter optimization to final assembly, takes only 1.5 hours, which is sufficiently short for most customized tasks.

B. Non-Constant Curvature Modeling

1) Kinematic Analysis: The proposed continuum robot is actuated by adjusting the length of the drive wire, denoted as ΔL, which is given by

$$\Delta L = \sum_{i=0}^{n-1} \Delta l_i, \tag{1}$$

where n is the number of joints in the continuum robot. The length change Δl_i of the drive wire can be expressed as $\Delta l_i = l_i^0 - l_i^b$, where l_i^0 is the length of the drive wire in the straight state and l_i^b is the length of the drive wire in the bending state. The straight-state length l_i^0 can be obtained by $\|\boldsymbol{v}_i^0\|_2$, and the bending-state length l_i^b is given by $\|\boldsymbol{v}_i^b\|_2$. Here, $\boldsymbol{v}_i^0$ and $\boldsymbol{v}_i^b$ are the vectors from point A to point B (in the straight state) and from point A to point B' (in the bending state), respectively, as shown in Fig. 2. These vectors can be solved as follows:

$$\boldsymbol{v}_i^0 = \begin{bmatrix} r_w\cos(\Delta\alpha_i) - r_w & -r_w\sin(\Delta\alpha_i) & l_0^s \end{bmatrix}, \tag{2}$$

$$\boldsymbol{v}_i^b = \boldsymbol{R}_y(\theta_i) \begin{bmatrix} r_w\cos(\Delta\alpha_i) \\ -r_w\sin(\Delta\alpha_i) \\ h_d \end{bmatrix} + \begin{bmatrix} -r_w \\ 0 \\ h_p \end{bmatrix}, \tag{3}$$

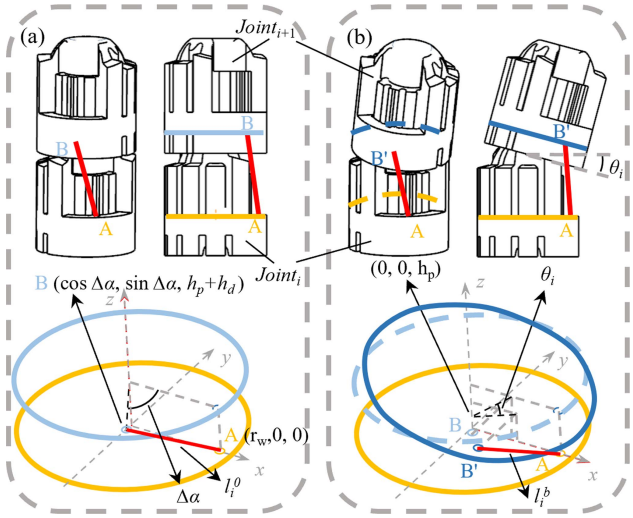

Fig. 2. Kinematic diagram of the continuum robot in (a) the straight state and (b) the bending state. The red line, which connects point A in $joint_i$ and point B in $joint_{i+1}$, represents the drive wire, whose length determines the rotation angle θ_i of $joint_{i+1}$. The orange circle, light blue circle, and blue circle represent $joint_i$, $joint_{i+1}$ in the straight state, and $joint_{i+1}$ in the bending state, respectively. The coordinates of the rotation center of $joint_{i+1}$ are $(0, 0, h_p)$.

where r_w denotes the distance between the centers of joints and holes through drive wire, and h_d and h_p represent the distance from the hinge center to the centers of $joint_i$ and $joint_{i+1}$, respectively, as shown in Fig. 2. $l_0^s = h_d + h_p$, and $\Delta\alpha_i = \alpha_{i+1} - \alpha_i$. The rotation matrix $\boldsymbol{R}_{axis}(\theta_i)$ denotes a rotation by an angle θ_i about the axis of rotation, where the axis (roll, pitch or yaw) is represented by x, y, or z, respectively. When $\Delta\alpha_i = 0$, the length change Δl_i^0 simplifies to $\Delta l_i^0 = l_0^s - (r_d^2 + r_p^2 - 2r_d r_p\cos(\theta_i^0 - \theta_i))$, where $r_d = \sqrt{h_d^2 + r_w^2}$, $r_p = \sqrt{h_p^2 + r_w^2}$, and $\theta_i^0 = \arccos((r_w^2 - h_d h_p)/(r_d r_p))$.

2) Potential Energy Analysis: The sensitivity of the proposed continuum robot can be derived using the minimum total potential energy principle.

The work W_f done by external forces can be expressed by

$$W_f = \sum_{i=0}^{n-1} \int F_i d\Delta l_i, \tag{4}$$

where F_i is the force exerted by the wire on the $joint_i$. The pulling force at $joint_i$ experiences a loss as the drive wire passes through the holes in the joints. The resulting force F_i at joint $joint_i$ can be quantified using the capstan equation:

$$F_i = \prod_{j=0}^{i} F_0 e^{-\mu_{wp}\varphi_j}, \tag{5}$$

where μ_{wp} denotes the coefficient of friction between the wire and the joints, and φ_i represents the total angle swept by the wire at the edge of $joint_i$. The efficacy of the pulling force loss was validated through experiments. And we have

$$\varphi_i = \arccos\left(\frac{\boldsymbol{v}_i^b \cdot \boldsymbol{v}_i^u}{|\boldsymbol{v}_i^b||\boldsymbol{v}_i^u|}\right) + \arccos\left(\frac{\boldsymbol{v}_i^b \cdot \boldsymbol{v}_i^l}{|\boldsymbol{v}_i^b||\boldsymbol{v}_i^l|}\right), \tag{6}$$

IEEE Robotics and Automation Letters (RA-L) paper, presented at ICRA 2026, Vienna, Austria. Cite as RA-L paper.

where $\boldsymbol{v}_i^l = [0 \quad 0 \quad 1]^T$ and $\boldsymbol{v}_i^u = \boldsymbol{R}_y(\theta_i)\boldsymbol{v}_i^l + [0 \quad 0 \quad h_p]^T$ are the normal vectors of the XY plane in the coordinate systems of $joint_i$ and $joint_{i+1}$, respectively.

According to previous research [13], the torque generated by the three guide wires, which serve as the backbones of the continuum robot, between $joint_i$ and $joint_{i+1}$ is given by

$$M_{bi} = \sum_{j=1}^{3} \frac{E_{nt} G_{nt} \pi {r_{nt}}^4}{E_{nt} + 2G_{nt}} \boldsymbol{\kappa_i^j}, \tag{7}$$

where E_{nt}, G_{nt} and r_{nt} are the elastic modulus, shear modulus and radius of guide wire, respectively. The sum of the curvature $\boldsymbol{\kappa_i^j}$ of guide wires is computed by $\sum_{j=1}^{3} \boldsymbol{\kappa_i^j} = 3\theta_i / l_0^s$. Total elastic potential energy in the continuum robot is

$$U = \sum_{i=0}^{n-1} \int M_{bi} \cdot d\theta_i. \tag{8}$$

The total potential energy $\boldsymbol{\Pi}$ of bent continuum robot can be expressed as

$$\boldsymbol{\Pi} = U - W_f. \tag{9}$$

Based on the principle of minimum total potential energy, the equation can be derived as follows:

$$\frac{\partial \boldsymbol{\Pi}}{\partial \theta_i} = 0. \tag{10}$$

Thus, giving external force F_0, bending angle θ_i of each joint can be determined using (4), (8), and (10). Consequently, the overall shape of continuum robot can be reconstructed.

C. Parameter Optimization

1) Forward Kinematics: By adjusting the parameters α_i and $\theta_{i\max}$, we can generate curves with the continuum robot that match our desired shape. A set of α_i and $\theta_{i\max}$ $(i = 0, 1, \ldots, n-1)$ values can define $n+1$ points starting from the origin. The coordinate of i-th joint is defined as $point_i(x_i, y_i, z_i)$. The rotation quaternion ${}^i\hat{\boldsymbol{q}}_{i+1}$ and translation vector $\boldsymbol{v}_i^t$ between neighboring points can be expressed as follows:

$${}^i\hat{\boldsymbol{q}}_{i+1} = (\theta_i, \boldsymbol{v}_i^r), \tag{11}$$

$$\boldsymbol{v}_i^t = (0, 0, l_0^s), \tag{12}$$

where $\boldsymbol{v}_i^r = (\cos\alpha_i, -\sin\alpha_i, 0)$ represents the rotation vector from $joint_i$ to $joint_{i+1}$, and θ_i is the rotation angle from $point_i$ to $point_{i+1}$ around the rotation vector $\boldsymbol{v}_i^r$. Thus, the coordinate transformation between $point_i$ and $point_{i+1}$ is governed by the dual quaternion, which is given by

$${}^i\hat{\boldsymbol{dq}}_{i+1} = ({}^i\hat{\boldsymbol{q}}_{i+1}, \boldsymbol{v}_i^t). \tag{13}$$

The dual quaternion from $point_0$ to $point_i$ can be obtained by ${}^0\hat{\boldsymbol{dq}}_i = \prod_{n=1}^{i} ({}^{n-1}\hat{\boldsymbol{dq}}_n)$. Therefore, each coordinate in the continuum robot can be calculated by

$$\hat{\boldsymbol{P}}_i = {}^0\hat{\boldsymbol{dq}}_i \hat{\boldsymbol{P}}_0 ({}^0\overline{\hat{\boldsymbol{dq}}_i}^*), \tag{14}$$

where ${}^0\overline{\hat{\boldsymbol{dq}}_i}^*$ is the dual conjugate of the dual quaternion ${}^0\hat{\boldsymbol{dq}}_i$. The dual quaternion $\hat{\boldsymbol{P}}_i$ for the i-th point is expressed as $1 + \varepsilon(x_i\boldsymbol{i} + y_i\boldsymbol{j} + z_i\boldsymbol{k})$, where ε is the dual unit and $\boldsymbol{i}$, $\boldsymbol{j}$, and $\boldsymbol{k}$ are the quaternion units.

Algorithm 1: Search of Key Parameters.

Input: $\widetilde{\boldsymbol{\alpha}} = (\widetilde{\alpha}_0, \widetilde{\alpha}_1, \ldots, \widetilde{\alpha}_{n-1})$,
$\widetilde{\boldsymbol{\theta}}_{\max} = (\widetilde{\theta}_{0\max}, \widetilde{\theta}_{1\max}, \ldots, \widetilde{\theta}_{(n-1)\max})$.
Output: d_{sum}

```
d_min ← d_sum
while d_sum ≤ d_min do
  for i ← 0 to n − 1 do
    α_i ← α̃_i ± k · α_step
    θ_{i max} ← θ̃_{i max} ± k · θ_step
    Solve FK to get d_sum
    d_min ← min(d_sum, d_min)
  end for
end while
```

2) Inverse Kinematics: To generate the desired curve using the proposed continuum robot, we introduce a design strategy to optimize the key parameters of the robot, as illustrated in Fig. 1. The procedure consists of the following steps:

Equidistant Sampling: Sample the desired curve equidistantly, where the sampling distance is equal to the length of the modular joints.

Coordinate Transformation: Apply coordinate transformation to the sampled points using dual quaternions. The transformation yields the desired values $\hat{\alpha}_i$ and $\hat{\theta}_i$ for the key parameters of the continuum robot.

Adjustment Based on Physical Constraints: Round off and adjust $\hat{\alpha}_i$ and $\hat{\theta}_i$ based on physical constraints to obtain feasible values for $\widetilde{\alpha}_i$ and $\widetilde{\theta}_{i\max}$ in the prototype. These values serve as the initial input for the optimization process. The constraints during the optimization are

$$\begin{aligned} \Delta\widetilde{\alpha}_i &\le \Delta\alpha_{limit}, \\ \widetilde{\theta}_{i\max} &\le \theta_{limit}, \end{aligned} \tag{15}$$

where $\Delta\alpha_{limit}$ is introduced to mitigate the significant loss of pull force from the drive wire as $\Delta\widetilde{\alpha}_i$ increases. θ_{limit} is determined by the physical constraints of the joint design.

Optimization Objective: The goal is to optimize the $\widetilde{\alpha}_i$ and $\widetilde{\theta}_{i\max}$ to minimize the sum of Euclidean distances, denoted as d_{sum}, between the points on the optimized curve and the desired curve. This optimization objective d_{sum} is described by the following equation:

$$d_{sum} = \omega d_m + (1 - \omega) d_e, \tag{16}$$

where ω is a weight factor balancing the global shape error d_m and the end-point error d_e, $d_m = (\sum_{i=0}^{n-1} \|\boldsymbol{p}_i^s - \boldsymbol{p}_i^d\|_2)/n$, and $d_e = \|\boldsymbol{p}_{n-1}^s - \boldsymbol{p}_{n-1}^d\|_2$. $\boldsymbol{p}_i^s$ and $\boldsymbol{p}_i^d$ represent the coordinates of the i-th point in the simulated and desired curve, respectively.

As shown in Algorithm 1, the search process involves sampling the k-nearest neighbors of $\widetilde{\alpha}_i$ and $\widetilde{\theta}_{i\max}$ to find the minium d_{sum}. The parameter spaces α_{step} and the θ_{step} define the feasible values for the modular joints' design. Furthermore, advanced optimization algorithms, such as genetic algorithms

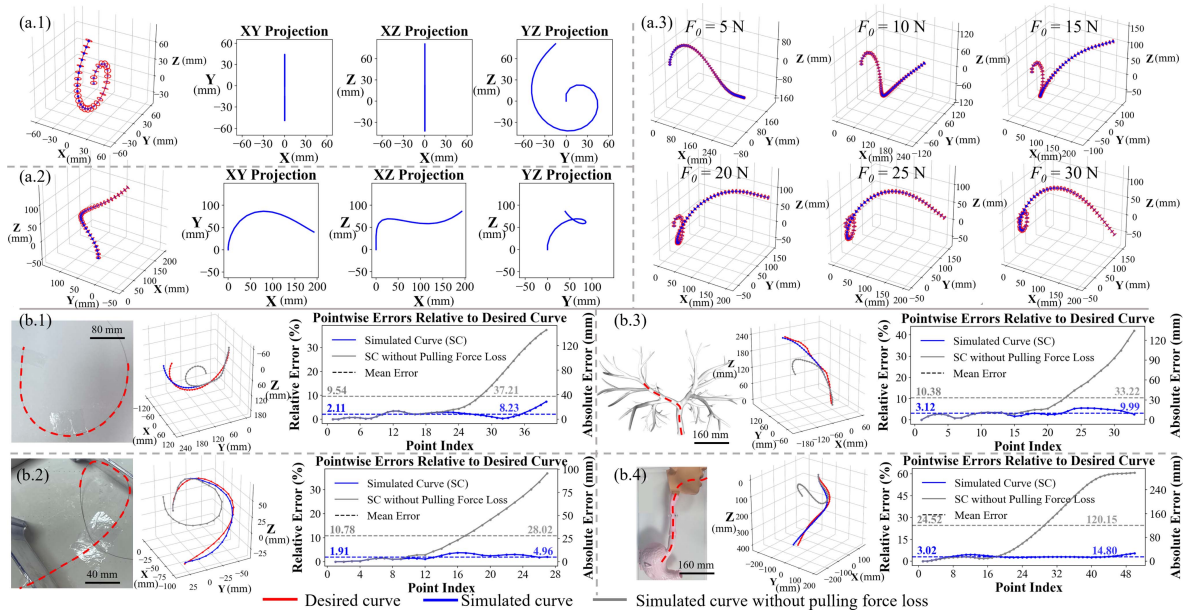

Fig. 3. Results of simulation experiments. (a) Forward design of the proposed continuum robot: (a.1) A logarithmic spiral shape with $F_0 = 10$ N, $\alpha_i = 0$, and $\theta_{i\max} = 45 - 1.5i$ $(i = 0, 1, 2, \ldots, 29)$; (a.2) A shape designed with $F_0 = 10$ N, $\alpha_i = 15 \times \lfloor i/2 \rfloor$, and $\theta_{i\max} = 15$ $(i = 0, 1, 2, \ldots, 29)$, based on the eight modular joints described in Section II-D; (a.3) Generated shapes under different values of F_0 with $\alpha_i = 10 \times \lfloor i/3 \rfloor$ and $\theta_{i\max} = 45 - 5 \times \lfloor i/5 \rfloor$ $(i = 0, 1, 2, \ldots, 49)$. (b) Curve-fitting experiments for (b.1) a 2D curve with a length of 390 mm, (b.2) a 3D curve with a length of 260 mm, (b.3) a bronchus curve with a length of 320 mm, and (b.4) a gastroscopic curve with a length of 490 mm. The relative error is calculated as $\|P_i^d - P_i^s\|_2 / l_c$, where P_i^d and P_i^s denote the coordinates of the i-th point in the desired and simulated curves, respectively, and l_c is the length of the desired curve.

and particle swarm optimization, can be integrated to enhance the optimization process. These methods offer significant potential for improving performance and can be thoroughly investigated alongside other optimization techniques to explore their comparative advantages and limitations.

D. Prototype

The modular joints and most components of the driving unit in the proposed programmable continuum robot can be manufactured using 3D-printed resin. The drive wire and guide wires are made of nitinol, with diameters of 0.3 mm and 0.5 mm, respectively. A Maxon motor is used to actuate the proposed continuum robot. Additionally, all other components are standard parts that are readily available for purchase.

The key parameters α and θ of modular joints have ranges of $[0, 360°]$ and $[0, 45°]$, respectively, with $\alpha_{step} = \theta_{step} = 15°$. These values determine the number of modular joint configurations, yielding a total of 8 distinct types. This includes 2 variations for α and 4 variations for θ. Further subdividing α_{step} and θ_{step} would greatly increase the number of modular joint types, which is unnecessary, as it does not lead to a significant reduction in the curve fitting error. Therefore, α_{step} and θ_{step} are set as an empirical value of 15°. Compared with previous continuum robot modular designs, whose modular joints must be assembled from multiple parts resulting in larger overall size, the proposed modular joints feature an integrated structure that allows their use in smaller and more spatially constrained environments.

Once a set of α_i and $\theta_{i\max}$ values is obtained, the continuum robot can be assembled. First, the modular joints are arranged in the optimized sequence. Next, all joints are connected by passing the drive wire through the drive holes. After that, each joint is rotated and its corresponding guide holes are connected using the guide wires. Finally, the drive wire is wound onto the drive pulley of the driving unit. The customization process can be performed by trained operators.

III. Results

A. Simulation Experiments

1) Forward Design: The proposed continuum robots can be easily designed by inputting α and $\theta_{\max}$. Given pulling force F_0 and a set of values for α and $\theta_{\max}$, specific shapes can be generated, such as the logarithmic spiral shape [26] shown in Fig. 3(a.1). The input values of α and $\theta_{\max}$ can theoretically take any consecutive values within range of $[0, 360°]$ and $[0, 45°]$, as specified by (15), providing a large design space.

Although α and $\theta_{\max}$, defined by (15) in the ranges $[0, 360°]$ and $[0, 45°]$, are feasible, the value of α_{step} and θ_{step} are inversely proportional to the number of types of modular joints, which in turn affects the design and manufacture costs. For example, while the α and $\theta_{\max}$ values are selected as described in Section II-D, the resulting shape is illustrated in Fig. 3(a.2). Both the shapes in Fig. 3(a.1) and (a.2) represent curves with non-constant curvature.

In addition to the parameters α and $\theta_{\max}$, the pulling force F_0 also affects the shape of the continuum robot. For instance, different values of F_0 produce distinct results, as shown in Fig. 3(a.3). For a continuum robot with a mininum diameter of 10 mm, the drive wire has a diameter of 0.3 mm, which limits the maximum allowable F_0 to prevent the drive wire from

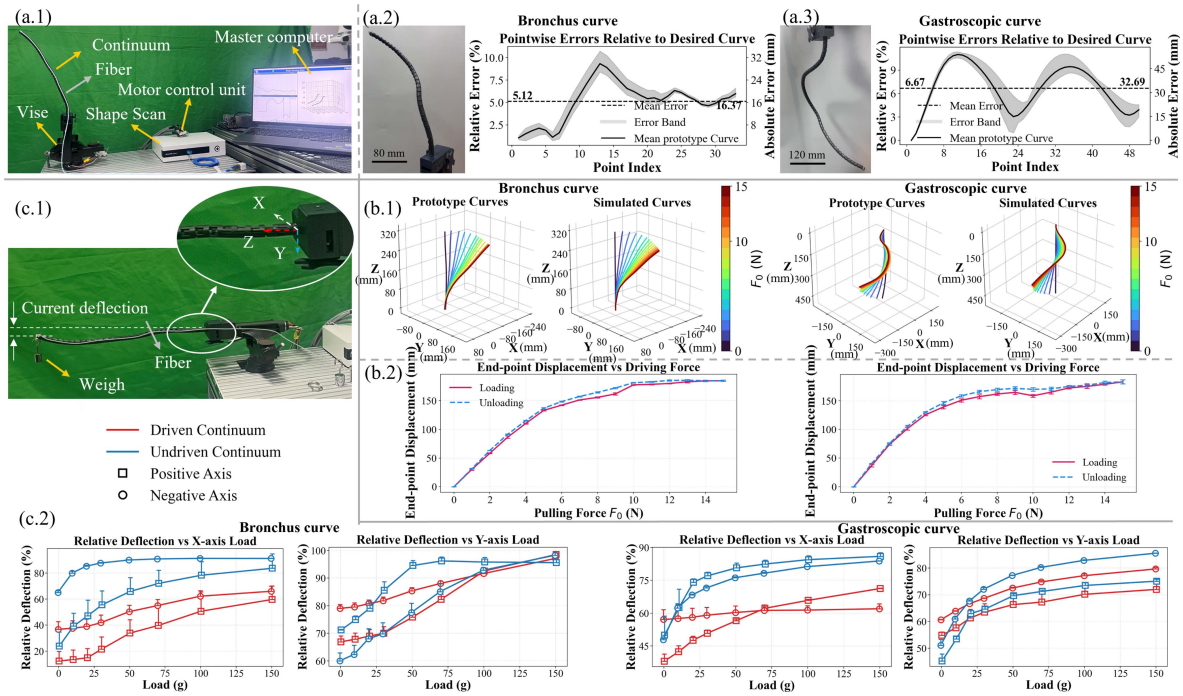

Fig. 4. Results of prototype experiments. (a) Kinematic performance of the proposed continuum robot prototype: (a.1) Experimental platform for sampling the continuum robot using embedded optical fiber sensors; (a.2) Pointwise errors between the prototype and the desired curves. The relative error is calculated as $\|P_i^d - P_i^p\|_2/l_c$, where P_i^p denotes the coordinates of the i-th point on the prototype curve. (b) Results of dynamic experiments for the prototype: (b.1) Prototype and simulated curves obtained when the continuum robot is driven by different F_0 values; (b.2) End-point displacement of the prototypes during loading and unloading. (c) Stiffness experiments of the prototypes: (c.1) Experimental platform for testing the stiffness of the prototypes, where loads are applied from different directions, namely the positive and negative directions of the X- and Y-axes; (c.2) Deflection characteristics of the prototypes. The relative deflection is calculated as $(\gamma_l - \gamma_i)/l_c$, where γ_l and γ_i represent the deflection of the prototype under loaded and unloaded conditions, respectively .

snapping. For larger continuum robots with a larger structure, this limitation on the pulling force can be relaxed, allowing for a broader range of variable values.

2) Curve Fitting: Curve fitting experiments were conducted to demonstrate the programmable trajectory-matching capability of the proposed design. Additionally, the theoretical model was validated through ablation analysis by comparing scenarios with and without consideration of pulling force loss (5). As shown in Fig. 3(b), four curves with distinct characteristics were tested. The bronchus curve was sampled from a bronchial mesh model, while the remaining curves were obtained using an optical fiber sensor (SHAPE A02-1050-N1, FBGS Technologies GmbH, Germany) and a shape scan (SHAPE-scan 901, FBGS, Germany). These reconstructed curves served as the ground-truth reference trajectories for evaluating the curve fitting performance. The four desired curves were fitted based on the method outlined in Section II-C2, with the pulling force loss (as discussed in Section II-B2) treated as a variable parameter in the experiments.

The experimental results, which include the desired curves, simulated curves accounting for pulling force loss, and simulated curves neglecting pulling force loss, are shown in Fig. 3(b). The simulated curves closely match the desired curves, with the relative mean error within 3.12%, and the relative end-point error within 7.41 %. Notably, when pulling force loss was incorporated into the non-constant curvature modeling based on (5), the curve fitting accuracy improved significantly. The mean Euclidean distances between the simulated and desired curves were reduced by at least three times, highlighting the importance of considering pulling force loss to achieve accurate curve fitting.

It can be observed that the errors in the 2D and 3D curves are lower compared to the bronchus and gastroscopic curves. This may be due to the smoother curvature and torsion of the 2D and 3D curves. Additionally, the error in the 2D curve increases significantly near the end-point, which is likely caused by the larger bending angle at the curve's end. These discrepancies are influenced by the physical constraints of the system, as discussed in Section IV.

B. Prototype Experiments

To further validate the proposed design, the performance of the prototypes in fitting the desired curves was tested. Based on the desired bronchus and gastroscopic curves described in Section III-A2, which served as the ground truth in the prototype experiments, two prototypes were fabricated. The prototype designed to fit the bronchus curve consists of 31 modular joints and has a total length of 320 mm, while the prototype designed to fit the gastroscopic curve consists of 48 modular joints and has a total length of 490 mm.

1) Fitting Characteristic: As shown in Fig. 4(a.1), the prototype was vertically fixed using a vise. An optical fiber sensor was embedded in the internal channel of the prototype to capture its shape, and a shape scanner was used to process the optical fiber data. The shape is sampled by the optical sensor data

IEEE Robotics and Automation Letters (RA-L) paper, presented at ICRA 2026, Vienna, Austria. Cite as RA-L paper.

corresponding to the length of the prototype. The system achieves an absolute wavelength accuracy of 10 pm and a repeatability (1σ) of 0.3 pm at full scan rate. During actuation with $F_0 = 10$ N to fit the desired curve, the shape of the prototype was recorded. Each experiment was repeated three times, and results are presented in Fig. 4(a.2).

There is a larger error in the prototype experiments compared to the simulation experiments, likely due to unmodeled energy losses, which will be discussed in Section IV. The mean relative errors of prototypes and desired curves were 5.12% and 6.67% for bronchus and gastroscopic curves, respectively, with relative end-point errors lower than 5.98%. These results are better than those reported in previous studies, where mean relative errors and relative end-point errors were 14% and 7% [17], 11% and 5% [23]. The prototype trajectories demonstrated close alignment with desired curves, thereby validating the design's feasibility and effectiveness.

2) Dynamic Performance: The prototypes were driven by different pulling forces F_0 to evaluate their dynamic performance. The experiments were conducted using the platform shown in Fig. 4(a.1). Compared with the experiments described in Section III-B1, the range of the pulling force F_0 was set to 0–15 N, and one experimental cycle consisted of gradually loading and then unloading the driving force. Each experiment was repeated three times.

The results of a representative experiment, in which F_0 increased from 0 to 15 N, are shown in Fig. 4(b.1). For both the bronchus and gastroscopic curves, the trajectories become denser as F_0 increases, indicating that each continuum robot has an upper limit for the applicable driving force. Based on empirical observations, 10 N was determined to be a suitable driving force for optimizing both the desired bronchus and gastroscopic curves. In addition, the prototype curves closely match the simulated curves as F_0 increases. By averaging three repeated experiments, the Root Mean Square Errors (RMSE) between the prototype and simulated curves were 6.81 mm and 13.61 mm for the bronchus and gastroscopic curves, respectively—sufficiently small for continuum robot performance.

The end-point displacements obtained from the three loading–unloading experiments are shown in Fig. 4(b.2). The prototypes exhibited good repeatability, with Standard Deviations (SD) of 1.67 mm and 4.77 mm for the bronchus and gastroscopic curves, respectively. Moreover, for the bronchus curve, the average and maximum hysteresis errors were 1.40% and 3.49% , while for the gastroscopic curve, they were 1.04% and 2.50% , respectively. For comparison, existing studies report average hysteresis errors of approximately 0.95% [27] and maximum errors of about 6.00% [28]. Therefore, the observed hysteresis errors are within a tolerable range for continuum robots.

3) Stiffness Characteristic: The stiffness of the proposed prototypes was tested to evaluate the system's performance and potential application scenarios. The testing platform is shown in Fig. 4(c.1). In the experiments, the continuum robot was fixed horizontally using a vise. Weights were then suspended from the distal joint of the robot, while its shape was continuously monitored and recorded using an optical fiber sensor embedded in the internal channel of the prototype. The driven force F_0 was set to 10 N. To comprehensively assess the stiffness response of the system, four loading directions were employed, namely, the negative and positive directions along the X-axis and Y-axis of the continuum robot's local coordinate system. Each experimental condition was tested three times to ensure the reliability and repeatability of the results.

The stiffness response was analyzed by measuring the relative deflection, as shown in Fig. 4(c.2). The initial deflection was nonzero due to the robot's self-weight. The SD of the repeated experiments were 7.95 mm and 3.55 mm for the bronchus and gastroscopic prototypes, respectively. It can be observed that the undriven continuum robots are highly compliant, whereas the driven prototypes are capable of resisting sub-newton-level forces. The stiffness of the driven prototypes was measured as 22.87 N/m and 25.87 N/m for the bronchus and gastroscopic curves, respectively. Although these stiffness values are relatively low and unsuitable for high-load environments, the prototypes can serve as pathways for other manipulators through their internal channels in low-load or non-contact scenarios. A deflection of less than 33% of the manipulator length under a 0.7 N load can be considered an adequate bending stiffness for surgical robotic applications [5], which is sufficient in most cases for the proposed prototypes. Furthermore, the prototypes can be supported by surrounding natural orifices during operation, which enhances their stability and adaptability.

IV. Discussion

A continuum robot with programmable tendon routing is proposed for generating desired 3D curves. Given a specific drive force F_0, the design space of the proposed continuum robot is the product of all possible combinations of $(\alpha, \theta_{\max})$, where the ranges of α and $\theta_{\max}$ are [0, 360°] and [0, 45°], respectively, subject to the constraints in (15).

Although the design space is large enough to accommodate many complex curves, the robot's ability to fit curves with sharp bends is limited due to physical constraints discussed in Section II-C2. The primary limitation arises from the friction between drive wire and joints, which is strongly influenced by $\Delta\alpha$. As a result, curves with inflection points are not ideal for the proposed continuum robot. To optimize the design, potential solutions include the use of lubrication or alternative drive mechanisms to reduce friction.

In addition to the pulling force loss and torque energy from the guide wires, there are other energy losses in the continuum robot system, including friction between the joints, friction between the joints and guide wires, and the system's gravitational potential energy. These factors are difficult to model because they are influenced by variables such as the 3D printing precision of the joints, the prototype's posture, and orientation. As a result, these unmodeled factors contribute to higher fitting errors in the prototype. Real-time calibration, achieved by detecting the prototype's shape and fine-tuning the pulling force of the drive wire, could be a potential solution to address these discrepancies.

Additionally, while the proposed modular joints with a diameter of 10 mm are suitable for most tasks, further miniaturization could enhance the versatility of the design method. Exploring

alternative joint connection methods to replace the articulated ball joints may provide potential solutions for improving the design.

This work focuses on the key parameters, namely yaw angle α and pitch angle θ, in the design of the continuum robot. In addition, several other decoupled design parameters can be considered, such as the distance between the centers of joints and the hole of drive wire [15], [23], the neutral line [29], and the bendable length [30]. Incorporating a broader range of variable parameters in the design and curve simulation of continuum robots could further enhance the system's dexterity and workspace, thereby providing more options for tackling a wider variety of specific tasks.

V. Conclusion

This letter introduces a novel continuum robot capable of generating desired 3D curves through a programmable tendon routing system. By optimizing the drive wire pathway within the modular joints to control rotational direction and angular deflection at each joint, the proposed continuum robot can generate precise curves using a single drive wire actuated by one motor, eliminating the need for complex and bulky drive systems. A non-constant curvature modeling approach is developed, and a parameter optimization method is presented to enable the robot to perform user-specific tasks effectively. The proposed system's performance is validated experimentally, demonstrating a relative mean error of less than 3.12% between simulated and desired curves. The prototype further exhibits a relative mean error of 6.67% from the desired curve.

This work introduces a novel approach to designing continuum robots, offering a pathway for improving existing designs and simplifying robotic systems, with potential applications in narrow, long passages such as natural orifice surgeries. Future research will focus on addressing the limitation of lacking online shape programmability and exploring more general design methods based on the proposed programmable continuum robot.

References

[1] J. Burgner-Kahrs, D. C. Rucker, and H. Choset, "Continuum robots for medical applications: A survey," *IEEE Trans. Robot.*, vol. 31, no. 6, pp. 1261–1280, Dec. 2015.

[2] M. Russo, N. Sriratanasak, W. Ba, X. Dong, A. Mohammad, and D. Axinte, "Cooperative continuum robots: Enhancing individual continuum arms by reconfiguring into a parallel manipulator," *IEEE Robot. Automat. Lett.*, vol. 7, no. 2, pp. 1558–1565, Apr. 2022.

[3] M. Russo et al., "Continuum robots: An overview," *Adv. Intell. Syst.*, vol. 5, 2023, Art. no. 2200367.

[4] A. Parra Rubio et al., "Modular morphing lattices for large-scale underwater continuum robotic structures," *Soft Robot.*, vol. 10, no. 4, pp. 724–736, Aug. 2023.

[5] X. Ma, X. Wang, Z. Zhang, P. Zhu, S. S. Cheng, and K. W. Samuel Au, "Design and experimental validation of a novel hybrid continuum robot with enhanced dexterity and manipulability in confined space," *IEEE/ASME Trans. Mechatron.*, vol. 28, no. 4, pp. 1826–1835, Aug. 2023.

[6] J. Rogatinsky et al., "A multifunctional soft robot for cardiac interventions," *Sci. Adv.*, vol. 9 2023, Art. no. eadi5559.

[7] Y. Kim, G. A. Parada, S. Liu, and X. Zhao, "Ferromagnetic soft continuum robots," *Sci. Robot.*, vol. 4, 2019, Art. no. eaax7329.

[8] A. Gao, N. Liu, M. Shen, M. E. M. K. Abdelaziz, B. Temelkuran, and G.-Z. Yang, "Laser-profiled continuum robot with integrated tension sensing for simultaneous shape and tip force estimation," *Soft Robot.*, vol. 7, pp. 421–443, Aug. 2020.

[9] P. Berthet-Rayne, K. Leibrandt, G. Gras, P. Fraisse, A. Crosnier, and G.-Z. Yang, "Inverse kinematics control methods for redundant snakelike robot teleoperation during minimally invasive surgery," *IEEE Robot. Automat. Lett.*, vol. 3, pp. 2501–2508, Jul. 2018.

[10] W. Hong, F. Feng, L. Xie, and G.-Z. Yang, "A two-segment continuum robot with piecewise stiffness for maxillary sinus surgery and its decoupling method," *IEEE/ASME Trans. Mechatron.*, vol. 27, no. 6, pp. 4440–4450, Dec. 2022.

[11] Y. Chitalia, S. Jeong, K. K. Yamamoto, J. J. Chern, and J. P. Desai, "Modeling and control of a 2-DoF meso-scale continuum robotic tool for pediatric neurosurgery," *IEEE Trans. Robot.*, vol. 37, pp. 520–531, Apr. 2021.

[12] W. Zeng, J. Yan, K. Yan, X. Huang, X. Wang, and S. S. Cheng, "Modeling a symmetrically-notched continuum neurosurgical robot with non-constant curvature and superelastic property," *IEEE Robot. Automat. Lett.*, vol. 6, no. 4, pp. 6489–6496, Oct. 2021.

[13] J. Wang, C. Hu, G. Ning, L. Ma, X. Zhang, and H. Liao, "A novel miniature spring-based continuum manipulator for minimally invasive surgery: Design and evaluation," *IEEE/ASME Trans. Mechatron.*, vol. 28, no. 5, pp. 2716–2727, Oct. 2023.

[14] Z. Xing, F. Wang, Y. Ji, D. McCoul, X. Wang, and J. Zhao, "A structure for fast stiffness-variation and omnidirectional-steering continuum manipulator," *IEEE Robot. Automat. Lett.*, vol. 6, no. 2, pp. 755–762, Apr. 2021.

[15] J. Li, Y. Zhou, J. Tan, Z. Wang, and H. Liu, "Design and modeling of a parallel shifted-routing cable-driven continuum manipulator for endometrial regeneration surgery," in *Proc. IEEE/RSJ Int. Conf. Intell. Robots Syst.*, Oct. 2020, pp. 3178–3183.

[16] J. Starke, E. Amanov, M. T. Chikhaoui, and J. Burgner-Kahrs, "On the merits of helical tendon routing in continuum robots," in *Proc. IEEE/RSJ Int. Conf. Intell. Robots Syst.*, Sep. 2017, pp. 6470–6476.

[17] A. Gao, H. Liu, Y. Zhou, Z. Yang, Z. Wang, and H. Li, "A cross-helical tendons actuated dexterous continuum manipulator," in *Proc. IEEE/RSJ Int. Conf. Intell. Robots Syst.*, Sep. 2015, pp. 2012–2017.

[18] D. C. Rucker and R. J. Webster Iii, "Statics and dynamics of continuum robots with general tendon routing and external loading," *IEEE Trans. Robot.*, vol. 27, no. 6, pp. 1033–1044, Dec. 2011.

[19] A. Gao, J. Li, Y. Zhou, Z. Wang, and H. Liu, "Modeling and task-oriented optimization of contact-aided continuum robots," *IEEE/ASME Trans. Mechatron.*, vol. 25, pp. 1444–1455, Jun. 2020.

[20] X. Ai, A. Gao, and W. Chen, "Dexterity comparison and analysis of multi-contact-aided continuum manipulators," *IEEE Robot. Automat. Lett.*, vol. 9, pp. 5679–5686, Jun. 2024.

[21] J. C. Case, E. L. White, V. SunSpiral, and R. Kramer-Bottiglio, "Reducing actuator requirements in continuum robots through optimized cable routing," *Soft Robot.*, vol. 5, pp. 109–118, Feb. 2018.

[22] J. Li et al., "Xstrings: 3D printing cable-driven mechanism for actuation, deformation, and manipulation," in *Proc. CHI Conf. Hum. Factors Comput. Syst.*, (Yokohama Japan), ACM, Apr. 2025, pp. 1–17.

[23] J. Barrientos-Diez, M. Russo, X. Dong, D. Axinte, and J. Kell, "Asymmetric continuum robots," *IEEE Robot. Automat. Lett.*, vol. 8, pp. 1279–1286, Mar. 2023.

[24] J. Zhang et al., "A preprogrammable continuum robot inspired by elephant trunk for dexterous manipulation," *Soft Robot.*, vol. 10, no. 3, pp. 636–646, Jun. 2023.

[25] L. Zhu, W. Xing, A. Song, and Y. J. Zhang, "Visibility-driven skeleton extraction from unstructured points," *Comput. Aided Geom. Des.*, vol. 82, 2020, Art. no. 101929.

[26] Z. Wang, N. M. Freris, and X. Wei, "SpiRobs: Logarithmic spiral-shaped robots for versatile grasping across scales," *Device*, vol. 3, 2024, Art. no. 100646.

[27] Y. Song, S. Wang, X. Luo, and C. Shi, "Design and optimization of a 3D printed distal flexible joint for endoscopic surgery," *IEEE Trans. Med. Robot. Bio.*, vol. 4, no. 1, pp. 38–49, Feb. 2022.

[28] J. Guo et al., "Kirigami-inspired 3D printable soft pneumatic actuators with multiple deformation modes for soft robotic applications," *Soft Robot.*, vol. 10, no. 4, pp. 737–748, 2023.

[29] J. Kim, S.-i. Kwon, Y. Moon, and K. Kim, "Cable-movable rolling joint to expand workspace under high external load in a hyper-redundant manipulator," *IEEE/ASME Trans. Mechatron.*, vol. 27, no. 1, pp. 501–512, Feb. 2022.

[30] B. Zhao, L. Zeng, Z. Wu, and K. Xu, "A continuum manipulator for continuously variable stiffness and its stiffness control formulation," *Mechanism Mach. Theory*, vol. 149, 2020, Art. no. 103746.